

Nonhysteretic behavior inside the hysteresis loop of VO₂ and its possible application in infrared imaging

M. Gurvitch,^{1,2} S. Luryi,^{1,3,a)} A. Polyakov,¹ and A. Shabalov¹

¹NY State Center for Advanced Sensor Technology (Sensor CAT), SUNY at Stony Brook, Stony Brook, New York 11794, USA

²Department of Physics and Astronomy, SUNY at Stony Brook, Stony Brook, New York 11794, USA

³Department of Electrical and Computer Engineering, SUNY at Stony Brook, Stony Brook, New York 11794, USA

(Received 2 June 2009; accepted 8 September 2009; published online 17 November 2009)

In the resistive phase transition in VO₂, temperature excursions taken from points on the major hysteresis loop produce minor loops. For sufficiently small excursions these minor loops degenerate into single-valued, nonhysteretic branches (NHBs) linear in $\log(\rho)$ versus T and having essentially the same or even higher temperature coefficient of resistance (TCR) as the semiconducting phase at room temperature. We explain this behavior based on the microscopic picture of percolating phases. Similar short NHBs are found in otherwise hysteretic optical reflectivity. We discuss the opportunities NHBs present for infrared imaging technology based on resistive microbolometers. It is possible to choose a NHB with 10^2 – 10^3 times smaller resistivity than in a pure semiconducting phase, thus providing a microbolometer operating without hysteresis, with low tunable resistivity, and high TCR. Unique features of the proposed method and projected figures of merit are discussed in the context of uncooled focal plane array IR visualization technology. © 2009 American Institute of Physics. [doi:10.1063/1.3243286]

I. INTRODUCTION

Technology providing for infrared (IR) imaging ability, of which night vision is the most obvious application, is of great current interest. In the past 2 decades this interest was primarily pursued by the military; civilian applications—a spin-off of military developments which were made public in 1992—abound as well. In its prevailing implementation, IR imaging in the atmospheric window 8–14 μm is based on large arrays of microbolometers (10^5 – 10^6 pixels) placed in a focal plane of IR optics, and operating at room temperature [uncooled focal plane array (UFPA) technology].^{1–4} Absorbed IR radiation changes the temperature of a microbolometer, which in turn changes its resistance, the latter being read out from each pixel, eventually being converted into a picture in the visible domain. Some of the relevant requirements are listed below:

- (1) In order to have high sensitivity, bolometers must have small thermal mass and be thermally isolated from their surroundings, which is achieved by placing them on suspended membranes (microbridges).
- (2) The sensing material must change its resistance with temperature, and the temperature coefficient of resistance (TCR) $\beta=(1/R)\Delta R/\Delta T$ characterizing such a change should be sufficiently high; here and in the rest of the paper R is resistance per square, related to resistivity of a sensor material ρ through $R=\rho/d$, where d is sensor film thickness.
- (3) Bolometer resistance R should be in the range appropriate for the resistive readout.
- (4) A bolometric sensor should absorb a large fraction of incident IR radiation.

- (5) IR radiation should be supplied to a sensor periodically rather than continually, in a modulated fashion, in order to have an opportunity to read out a signal and to start anew after each cycle, providing a time-dependent image of a scene. The frequency of this modulation (*frame frequency*), which is typically from 30 to 60 Hz, provides a continuous moving picture for a human eye.
- (6) The material of a sensor and other parts of the system should not produce large electronic noise. The last requirement is also implying a need for signal modulation, as $1/f$ noise would be very large at dc.

Let us write down the basic formulae^{1,5,6} describing a bolometric detector, in some cases modifying them to adapt to our needs in this paper. If the incident IR radiant power P_{IR} falling on a sensor is modulated with the angular frequency ω , the amplitude of periodic sensor temperature variation will be $\Delta T_s = \eta P_{\text{IR}} / (G^2 + \omega^2 C^2)^{1/2}$, where C is sensor heat capacity (also called the *thermal mass*), G its thermal conductance to the surroundings (principally to the substrate), and $0 < \eta < 1$ is a fraction of the incident power absorbed by the sensor (*absorptivity*). Once the input power is removed, the temperature disturbance decays exponentially with a characteristic time $\tau_{\text{th}} = C/G$, called the *thermal constant*. The typical τ_{th} in bolometric detectors is in the ms range, e.g., $\tau_{\text{th}} = 10$ ms. In terms of τ_{th} , the formula for the temperature amplitude (essentially, a low-pass filter formula) can be written in the form

$$\Delta T_s = \frac{\eta P_{\text{IR}}}{G \sqrt{1 + \omega^2 \tau_{\text{th}}^2}}. \quad (1)$$

A sensor may be also heated during an electrical readout, receiving the joule power $P_j = I_b^2 R$, where I_b is the bias current flowing through the sensor and R is its resistance. In

^{a)}Electronic mail: sluryi@ece.sunysb.edu.

order to sequentially read out a large number of sensors (pixels) in an array within one frame period, and to minimize sensor heating, the readout takes place in short pulses, with $\tau_r = 25\text{--}70 \mu\text{s}$.¹⁻⁴ In this case almost no energy escapes from a sensor during each pulse, and so the temperature increase during readout can be estimated from

$$\Delta T_r = I_b^2 R \tau_r / C. \quad (2)$$

A useful detector figure of merit is the *voltage responsivity* R_V , defined as the ratio of the output voltage signal amplitude $\Delta V = I_b \Delta R$ to the input radiant power P_{IR} , viz., $R_V = I_b \Delta R / P_{\text{IR}}$. It follows from the definition of $\beta = (1/R) \Delta R / \Delta T_s$ and from Eq. (1) that

$$R_V = \frac{\eta \beta I_b R}{G \sqrt{1 + \omega^2 \tau_{\text{th}}^2}}. \quad (3)$$

Here and in what follows we are taking absolute values of ΔR and β because in a semiconductor ΔR and β are negative. As can be seen from Eq. (3), R_V is mainly governed by the electrical (R and β) and thermal (G and C) properties of a sensor, but it does not include its noise characteristics. The remarkably small values of G and C achieved with modern on-wafer fabrication, coupled with reasonably high $\beta \approx 0.02 \text{ } ^\circ\text{C}^{-1}$, allowed the UFPA technology based on VO_x microbolometers¹⁻⁴ to reach the voltage responsivity as high as $R_V = 2.5 \times 10^5 \text{ V/W}$.

A sensor characteristic which encompasses both the R_V and the noise is NETD, the noise equivalent temperature difference. It appears as the most important figure of merit in virtually all of the reports of UFPA technology.¹⁻⁴ The meaning of NETD is transparent and easy to grasp: it is the smallest temperature difference on a *target* (scene) that can be detected by a sensor. Specifically, it is the temperature difference on a target ΔT_t which produces such an electrical signal ΔV in a sensor that it is equal to the sensor's total rms noise voltage $V_n(\Delta f)$ in the measurement bandwidth Δf . The latter is often taken as the inverse of $2\tau_r$,² but sometimes as a much more narrow range.⁶ If we take $\Delta f = 1/(2\tau_r)$, we will find $\Delta f = 7.14 \text{ kHz}$ for $\tau_r = 70 \mu\text{s}$.

If a sensor increases its temperature by ΔT_s , then $\Delta V = \beta R I_b \Delta T_s$, by the definition of β . The temperature difference on a target ΔT_t which produced ΔT_s is larger than ΔT_s . The ratio of the two can be measured when real sensors are available, or can be calculated, as we have done in Sec. VIII. We found by calculation $\psi = \Delta T_s / \Delta T_t \approx 0.01$ for the case of $F/\# = 1$ optics (aperture equals focal length) and for the typical sensor characteristics [see Sec. VIII]. Then $\Delta V = \psi \beta R I_b \Delta T_t$; equating this signal voltage with noise voltage $V_n(\Delta f)$ we find

$$\text{NETD} = V_n(\Delta f) / (\psi \beta R I_b). \quad (4)$$

Expressing NETD in terms of R_V we obtain

$$\text{NETD} = \frac{\eta V_n(\Delta f)}{\psi R_V G \sqrt{1 + \omega^2 \tau_{\text{th}}^2}}. \quad (5)$$

Therefore, the NETD and R_V are inversely proportional; a good sensor has both high R_V and low NETD. In the best cases, the values of NETD achieved in UFPA technology for

$50 \times 50 \mu\text{m}^2$ microbolometers are below 10 mK ;¹⁻⁴ values below 100 mK are considered respectable.

We will be using these formulae throughout the paper when arguing about various dependences, and in Secs. VIII and IX when making some estimates. In these estimates we will be taking typical values characterizing a sensor pixel in existing UFPA technology,¹⁻⁴ such as C , G , A , τ_{th} , etc. When different parameters emerging in the regime of operation discussed in this paper will be required, we will use them alongside these familiar ones.

II. SENSOR MATERIALS: VO_x AND VO_2

A long time ago there were proposals⁷ to operate the uncooled (even heated) bolometer as a transition-edge device using the strong semiconductor-to-metal phase transition (SMT), such as found in VO_2 at $68 \text{ } ^\circ\text{C}$ in single crystals⁸ and between 50 and $90 \text{ } ^\circ\text{C}$ in typical polycrystalline films.⁹ The SMT-based device was proposed as a high-temperature substitute for a superconducting transition-edge bolometer operating at low temperatures. Resistivity ρ is changing by a factor of $\sim 10^3\text{--}10^4$ in SMT in VO_2 films, providing high TCR ($\sim 100\% \text{ } ^\circ\text{C}^{-1}$) in the transition region and thus promising high bolometer responsivity [see Eq. (1)]. Variations and refinements of this attractive idea continue to reappear in the literature.^{10,11} Yet today's UFPA technology is based on resistive readout of individual VO_x microbolometers operating at or around room temperature,¹⁻⁴ away from the SMT in VO_2 . Usually the nonstoichiometric, mixed oxide VO_x films used in this technology do not possess SMT at all. The reason for abandoning the very high transition region TCR is that, unfortunately, it is accompanied by other undesirable features, of which the main culprit is the hysteresis, which greatly complicates sensor operation. There is also latent heat released/absorbed in the transition,⁸ which is feared to interfere with bolometer operation.² Also the fact that transition takes place at elevated temperatures requires heating of the bolometer above room temperature. There is also an issue of excess noise, which appears to increase in the phase transition region¹² and even at $25 \text{ } ^\circ\text{C}$ in the presence of a transition at higher temperatures¹³ (see Sec. X).

So, despite the high TCR in the transition region, the difficulties of having to deal with hysteresis, latent heat, elevated temperature of operation and excess noise proved to be too much for the developing technology, and proposals to use the phase transition were bypassed. Instead, a mixed vanadium oxide VO_x that has no phase transition was retained as a semiconductor sensor material because it was found to possess at or near room temperature ($25 \text{ } ^\circ\text{C}$) an attractive combination of reasonably high $\beta \approx -2\% \text{ } ^\circ\text{C}^{-1}$, relatively low $R \sim 10\text{--}200 \text{ k}\Omega$ in 50 nm films, and low excess $1/f$ noise.^{1-4,13} The development of low-temperature ($\leq 400 \text{ } ^\circ\text{C}$) ion beam sputter-deposition process for the preparation of VO_x was also significant in making this choice. Yet the fact that VO_x was chosen by the mainstream technology out of all the other possible choices of semiconducting sensor materials probably had something to do with vanadium oxide just "being there:" VO_2 turned into VO_x and remained the workhorse of UFPA technology.

It should be noted that, despite a fairly wide range of R values which can be obtained in VO_x , all practical UFPA devices utilize mainly $R \sim 10\text{--}20\text{ k}\Omega$,¹⁻⁴ as higher R cause problems in matching to the readout amplifiers, in sensor heating by the readout current [see Eq. (2) and Sec. VIII], and in producing Johnson's noise. The latter has been sometimes cited as the prevailing noise source even at $10\text{--}20\text{ k}\Omega$,¹ although one also finds alternative statements that $1/f$ noise is the prevailing noise source in VO_x bolometers; clearly, both noise sources are significant.

Thus, to summarize, the pure phase VO_2 is not used in today's UFPA technology because of (a) complications caused by the phase transition (mainly hysteresis) and (b) high pixel resistance R . This resistance mismatch is indeed severe: the resistivity ρ of a pure phase VO_2 ranges from 0.1 to $1.0\ \Omega\text{ m}$,⁹ corresponding to $R=2\text{--}20\text{ M}\Omega$ in a 50 nm film, which is $10^2\text{--}10^3$ times (!) higher than the acceptable range.

One cannot resolve this difficulty by making the sensing layer thicker. Needless to say, one cannot make it $10^2\text{--}10^3$ times thicker than 50 nm for technological reasons. Somewhat thicker films, e.g., with $d=250\text{ nm}$, can be made, but their utilization would not fully resolve the issue under consideration, while any increase in sensor thickness is undesirable as it increases the bolometer thermal mass C thus increasing $\tau_{\text{th}}=C/G$ and therefore reducing responsivity and increasing NETD, as follows from Eqs. (3) and (5).

Clearly, in a semiconductor, the requirements of high TCR and low $R=\rho/d$ are directly conflicting with each other. If the activation energy is $E_g/2$, half the bandgap in an intrinsic semiconductor, then

$$\rho = \rho_0 \exp(E_g/2kT),$$

$$\beta = d(\ln \rho/dT) = 1/\rho(d\rho/dT) = -E_g/2kT^2. \quad (6)$$

Higher values of E_g will increase both ρ and $|\beta|$. This dichotomy between the TCR and ρ in a semiconductor is clearly revealed in the numerous data collected in the literature on resistive properties of various VO_2 films. In our own work on films produced by the precursor oxidation process (POP) (Ref. 9) and by the pulsed laser deposition (PLD) (Ref. 14) we found for 50 nm films values of R in the megaohm range, while TCR varied from -2.5 to -5% $^\circ\text{C}^{-1}$. The conclusion reached by us in Ref. 9 (and by others before us) was that, despite an attractive TCR, the high R values make these films unsuitable for the resistive-readout IR imaging application.

We conjecture that, if it were not for the large resistance, the pure phase VO_2 would be preferred over VO_x for the sake of higher bolometer responsivity (TCR of $2.5\%\text{--}5\%$ versus 2%) and because a well-defined single phase sensor material would provide for an easier process control compared to a need to reproduce and make uniform layers of a mixed, ill-defined, and ill-behaved VO_x .

We mention these attractive features here because we have discovered a remarkable phenomenon which takes place in a pure phase VO_2 and offers the possibility of preserving and even further increasing the high TCR while both avoiding the hysteresis and dramatically lowering the R (by

orders of magnitude). As will be shown in detail below, we found the way of hysteresis-free operation of VO_2 films right in the region of their hysteretic transition. Moreover, our understanding of this new phenomenon indicates that its use circumvents some of the other difficulties associated with the phase transition, such as the emission/absorption of significant latent heat. Both Johnson's and excess noise, other conditions being equal, are lower in lower R films. An additional benefit which can be derived from operating a sensor in the hysteretic region, in the mixed phase, is the increased bolometer absorptivity η of IR radiation in the $8\text{--}14\ \mu\text{m}$ band. The need to operate at the temperatures above room temperature remains. We will discuss these issues in Sec. VIII. A short preliminary report of this work, lacking optical studies, noise measurements, and figure of merit estimates was published online.¹⁵

III. SAMPLE PREPARATION AND MEASUREMENTS

Our VO_2 films were deposited by POP (Ref. 9) at $400\text{ }^\circ\text{C}$ and by PLD (Ref. 14) at $600\text{--}650\text{ }^\circ\text{C}$. We recognize that, while $400\text{ }^\circ\text{C}$ is an acceptable preparation temperature in UFPA technology, $600\text{ }^\circ\text{C}$ may be too high. Nonetheless, we found it useful to study these two types of samples in order to gain insight into the phenomena which eventually may lead to applications of POP samples alone. Oxidized silicon and sapphire substrates were used in both deposition methods. Our films were polycrystalline with grain sizes from ~ 50 to $\sim 400\text{ nm}$, checked by electron microscopy. Judging by the resistivity and optical reflectivity behavior of PLD samples, and comparing them with our previously extensively studied POP samples,⁹ we believe them, as well as POP films, to be of essentially pure VO_2 phase. The resistance ratio between the semiconducting (S) and metallic (M) phases was up to 2×10^3 in the best POP films, while in PLD films it reached 5×10^3 on Si/SiO₂ and 4×10^4 on sapphire. Despite a superior resistance ratio found in PLD films, the hysteresis in PLD films was wider than in POP films. This difference may be related to different average grain sizes and unequal structural perfection. Additionally, hysteresis width is known to depend on film thickness; our POP films were 220 nm thick while PLD films were 95 nm thick.

Our interest in the detailed resistivity and optical reflectivity behavior in limited temperature intervals inside the major hysteresis loop of VO_2 required careful measurements. At the beginning of our studies we found significant problems measuring $\rho(T)$ due to a discrepancy between the thermometer reading and the true sample temperature. This led to systematic errors in measuring $\rho(T)$, with sample-thermometer temperature lag changing sign depending on whether the sample was heating or cooling. In measurements in which the direction of temperature change is being at some point reversed, this problem manifests itself as a false hysteresis: exactly the kind of thing we wanted to avoid given our specific interest. This systematic error in $\rho(T)$ measurement was found to depend on the rate of temperature sweep. To make sure that the data is free of such systematic errors, we performed the resistive measurements in two dis-

tinct modes described below, and the results were compared by measuring selected samples by both methods.

Method 1 served as a standard; it was performed in a “classical” resistivity-measuring arrangement, in a quasi-static regime, in a thermally shielded environment in which the sample and thermometer temperatures were given time to equilibrate. Even though measurements were performed in the temperature range from 25 to 100 °C and required no cooling, we found it convenient to mount our samples in the commercial Janis VPF-475 cryostat, which has a heater capable of reaching 100 °C. We took care to avoid a temperature differential between the embedded thermometer and the exposed film surface which can be cooled or heated by heat conduction, air convection, and radiation exchange with the environment. We used the techniques commonly employed in precise resistivity measurements. The sample was mounted on a massive copper block, which also contained a thermocouple thermometer. This block was enclosed in a thermal copper shield thermally linked to the block, the arrangement protecting against the abovementioned temperature differential problem. In some of the runs we also evacuated the cryostat to completely remove the convection and thermal conductivity through air (loss of oxygen from the film in vacuum was however a concern, and so this was not used routinely). Resistivity was measured using reliable indium contacts applied to a film configured in a four-probe geometry, with 0.4–4 μA measuring current. A Lakeshore 321 temperature controller swept the temperature at a rate of ≤ 0.5 °C/min, which was verified to produce true $\rho(T)$ measurements. Higher rates produced the temperature lag described above. The data points were collected with the use of an automated measuring system based on LABORATORY VIEW software.

Fixed-wavelength optical reflectivity versus temperature $R_\lambda(T)$ measurements were performed with a Perkin–Elmer UV/VIS Lambda 20 spectrometer, in the wavelength λ range from 200 to 1000 nm. We used the same temperature controller as in resistivity measurements, and employed the “time-drive” mode available in the Lambda 20 spectrometer. The latter means that spectrometer measures reflectivity at a fixed λ as a function of time, while sweeping the temperature over the desired range, with temperature being proportional to time. Reflectivity $R_\lambda(T)$ can be reconstructed from these measurements.

The second measurement technique (method 2) was developed later in the program. The setup used in method 2 had the great advantage of being able to measure resistivity and reflectivity simultaneously and at the same location. The four-spring-loaded gold-plated probes for resistivity measurement were placed at regular 3 mm intervals. The two outer probes delivered measuring current from 0.4 to 4 μA . R was calculated using the formula and corrections provided in Ref. 16. For probes placed on a large (“infinite”) film area, one has $R = (\pi/\ln 2)V/I = 4.53V/I$, where I and V are, respectively, the measuring current and the voltage appearing between the inner probes. If the distance between voltage probes is S , and the film around the probes can be assumed to

be approximately circular with diameter D , the ratio D/S defines a multiplicative correction,¹⁶ which in our case was approximately 0.92, making $R = 4.17V/I$.

A custom made 1 mm diameter optical reflectivity probe consisting of five light-source fibers bundled around one measurement fiber was utilized to illuminate the sample and to measure the reflectivity of a small spot located between the voltage probes. A broad band combined halogen and deuterium light source (Ocean Optics DH-2000 BAL) was used to launch light into the five source fibers, while the light from the central sensing fiber was routed to an Ocean Optics Spectrometer HR2000CG capable of measuring reflectivity in the wavelength range from 200 to 1100 nm. This spectrometer was somewhat noisier than the Perkin–Elmer UV/VIS Lambda 20 spectrometer, but it was more convenient to use in combination with resistivity measurements. The temperature was controlled using a Lakeshore 325 controller driving a resistive heater. Computer controlled fans were used to cool the sample mounting plate at higher ramp rates. Temperature measurements were made with a Chromel–Alumel thermocouple placed on the heated stage. A special draft shield was built to reduce thermal drift due to air currents. The entire setup was operated under computer control which included control of the temperature ramp rates. The accuracy of the measurements thus obtained was verified by comparing to the measurements on the same sample done in the quasistatic regime (method 1). While in our previous publications^{9,15} all measurements were performed by method 1, most of the figures shown in this paper were obtained by method 2. We will note the use of method 1 when it appears in this paper.

The relevant resistance in applications is that of a pixel, which is square in shape, and hence equal to $R = \rho/d$. In this paper we are presenting resistivity data as $\log R$ versus T . We provide film thickness d alongside R , so that resistivity ρ can be readily obtained from these data. With this understanding, we traditionally refer to these data as the “resistivity,” sometimes denoted by $\rho(T)$.

In Fig. 1 we superimposed several resistivity measurements performed by method 2. We show a major hysteresis loop in VO_2 traced at sweep rates differing by a factor of 200, from 0.1 to 20 °C/min.

An inset in Fig. 1, referring to the point around the highest major loop (ML) slope at 75 °C, shows observed $|\Delta T|$ shifts between the resistivity curves measured at different sweep rates, taking the 0.1 °C/min curve as a reference. The shift corresponding to 1 °C/min is 0.05 °C, the shift at rates of 5 and 10 °C/min is $\Delta T \approx 0.3$ °C, and the shift at 20 °C/min is $\Delta T \approx 0.65$ °C. These shifts (systematic errors) may or may not be acceptable, depending on the set goals. We used 5 °C/min as a fast sweep rate for quickly measuring the overall behavior on the ML scale, considering a systematic error of 0.3 °C as acceptable on such a large scale. When studying the behavior on a finer scale we used 0.1–1 °C/min rate in method 2 and 0.5 °C/min rate in method 1. We will note sweep rates in figure captions when presenting the data.

Systematic errors described above should be distinguished from real transition-region instabilities. In this work

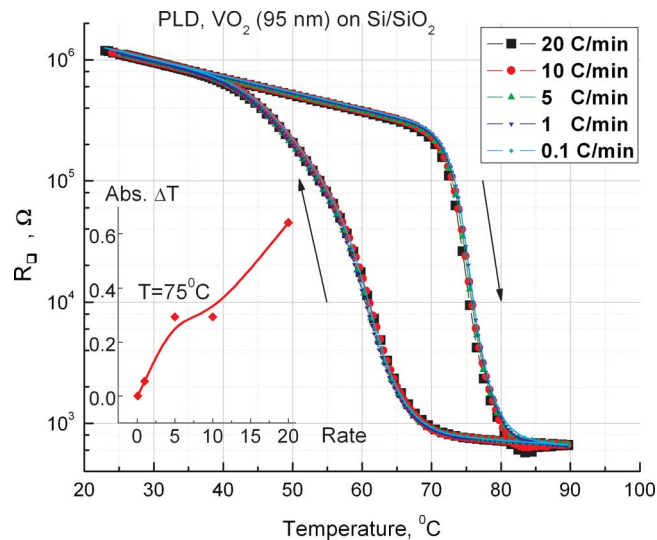


FIG. 1. (Color online) Major hysteresis loop of a PLD sample ($d = 95$ nm), measured at temperature sweep rates from 0.1 to 20 °C/min, illustrating how different rates of heating/cooling influence the resistivity measurement in method 2.

and in our previous study⁹ we sometimes observed small but real resistivity shifts in repeated cycling of VO₂ films. This included diminishing successive shifts observed in repeated measurements of the same part of the resistivity curve, a phenomenon which was also observed and called *accommodation* in Ref. 17. We found that instability in as-made films can be significantly reduced by employing prolonged postanneals and sample “training” via repeated temperature cycling. We adopted a 36 h anneal in air at 120–130 °C which largely stabilized our films. In some cases we also covered them with photoresist for protection from further oxidation or from loss of oxygen. Obviously, resistive instability is unwelcome in applications. The full extent of this problem when dealing with VO₂ in the transition region and the methods of its removal should be studied further.

We have also measured noise in our films. Details of that measurement are given in Sec. X.

IV. NONHYSTERETIC BEHAVIOR INSIDE THE HYSTERESIS LOOP

Temperature excursions from an *attachment point* on a side of a major hysteresis loop produce minor or nested loops.^{17,18} These smaller loops are also hysteretic. When the excursion length is equal or greater than the major hysteresis loop width, minor loops are as wide as the ML, while covering smaller resistivity range.^{17,18} When the excursion length is smaller than the ML width, minor loops are smaller than the ML both in resistivity range and in temperature width.

We note that the nature of a hysteresis phenomena dictates that a minor loop can be produced starting from any *attachment temperature* T_0 on the ML only in a certain way, namely, by making a *backward round-trip excursion* from that temperature. For T_0 on the heating branch (HB) the backward roundtrip excursion denotes a $T_0 \rightarrow T_0 - \Delta T \rightarrow T_0$ process, i.e., cooling down from T_0 to $T_0 - \Delta T$ and then warming up by ΔT back to T_0 . Here and below we will

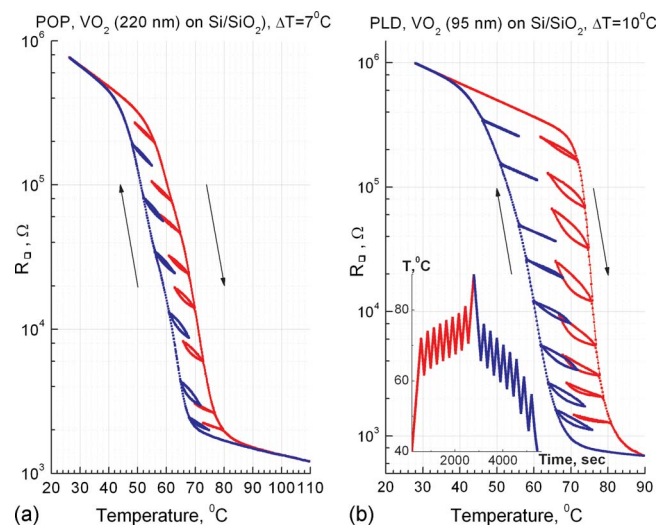


FIG. 2. (Color online) (a) POP sample ($d = 220$ nm) and (b) PLD sample ($d = 95$ nm). MLs are shown with a number of minor loops attached at different points on the HBs and CBs indicated by arrows (and shown in red and blue respectively when colors are available), the *excursion length* of minor loops is $\Delta T = 7$ °C in a POP sample and 10 °C in a PLD sample. The inset in (b) shows how the temperature was ramped in order to measure the plurality of NHBs on the ML; ramp rate was 5 °C/min.

always assume that $\Delta T > 0$; we shall refer to a positive quantity ΔT as an *excursion length*, or simply as an *excursion*. On the cooling branch (CB) the backward direction is that of warming up, and so the backward roundtrip excursion is $T_0 \rightarrow T_0 + \Delta T \rightarrow T_0$. Excursions in the opposite (forward) direction on either HB or on CB do not produce minor loops. Instead they produce, upon return to the initial temperature, a changed value of a measured quantity (such as resistivity or optical reflectivity), which sometimes is referred to as a “memory” effect.

We became interested in studying minor loops with reduced excursion length. In Figs. 2(a) and 2(b) we show major resistivity loops of POP and PLD samples with minor loops attached at regular intervals, these minor loops having widths (*excursion lengths*) of $\Delta T = 7$ °C and 10 °C in POP and PLD samples, respectively.

We can see that most of the minor loops in Figs. 2(a) and 2(b) are hysteretic, but we also notice that some of them are rather flat. The loops near the semiconducting and metallic ends of the ML are flatter than the loops in the middle of the hysteretic region.

We studied minor loops with progressively smaller excursions ΔT . We discovered that for sufficiently small ΔT , minor loops flattened out, degenerating into what we call *nonhysteretic branches* (NHBs). Although some minor loops may become flat even at ~ 10 °C, as can be seen in Fig. 2(b), all of them become flat below $\Delta T^* \approx 5$ °C (see Fig. 3).

A NHB can be initiated from any attachment point on the ML, either on a HB or on a CB. Another prominent feature of NHBs evident from Figs. 3 is that they are linear in $\log(\rho)$ versus T and that most of them have the TCR of the semiconducting phase (i.e., the room-temperature TCR), or even higher, except for the NHBs on a HB that are close to the merging point (metallic phase end) of the ML, the latter having visibly lower TCRs. We will discuss the physical reasons for this behavior below.

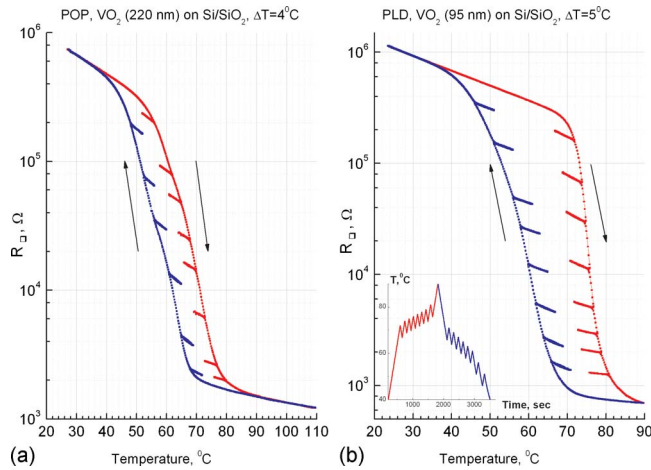


FIG. 3. (Color online) (a) POP and (b) PLD samples (same as in Figs. 2) measured with shorter excursions $\Delta T=4^\circ\text{C}$ and $\Delta T=5^\circ\text{C}$, respectively. The inset in (b) shows how the temperature was ramped in order to measure the plurality of NHBs on the ML; ramp rate was $5^\circ\text{C}/\text{min}$.

We traced a number of different NHBs back and forth within ΔT^* , measuring them with both methods 1 and 2, and plotting the results on expanded R -scales. To the precision of our measurements, they were single valued and linear in $\log(\rho)$ versus T . Two representative NHBs, measured in round-trip excursions, are plotted in Fig. 4 on expanded scales.

V. NHBs AND THEIR TCRs AROUND THE ML

Examination of Figs. 3(a) and 3(b) suggests that, except for the region close to the high-temperature merging point of the ML $T_M \approx 90^\circ\text{C}$, all NHBs exhibit similar slopes on the $\log(\rho)$ versus T plot, i.e., similar β , and that these slopes are similar to the slope in the semiconductor (S) phase below the phase transition. This similarity, in our opinion, strongly points to the underlying cause of semiconducting behavior in NHBs being the electrical conduction through the *percolat-*

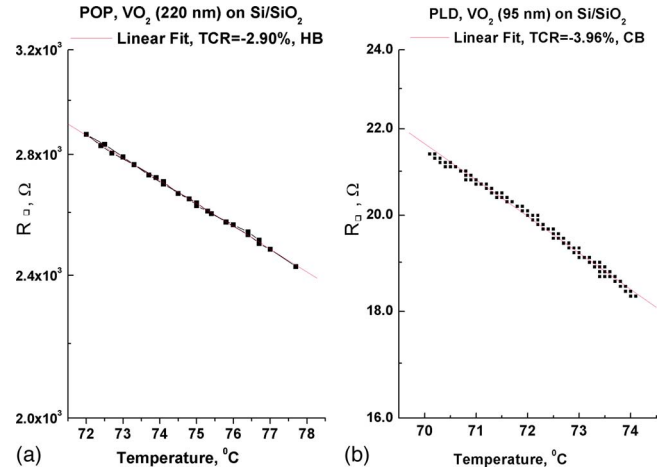


FIG. 4. (Color online) NHBs from POP and PLD samples on expanded scales; linear fits to $\log R$ vs T are shown, and corresponding TCR values are indicated. (a) POP sample, HB, $T_0=77.7^\circ\text{C}$. (b) PLD sample, CB, $T_0=70.0^\circ\text{C}$. Method 1, ramp is $0.5^\circ\text{C}/\text{min}$.

ing semiconducting phase, as will be discussed in more detail below.

The actual TCRs obtained by fitting NHBs of Fig. 3 are plotted versus T_0 in Figs. 5(a) and 5(b), for both HB and CB of the POP [in Fig. 5(a)] and PLD [in Fig. 5(b)] samples. Here we are discussing TCRs [triangles and squares in Figs. 5(a) and 5(b)]; the optical reflectivity slopes plotted on the same graph will be discussed in Sec. VI.

We note that TCRs in S-phase at 25°C in our POP and PLD samples are $3.5\%^\circ\text{C}^{-1}$ and $3.13\%^\circ\text{C}^{-1}$, respectively, which is considerably higher than typical $\text{TCR} \approx 2\%^\circ\text{C}^{-1}$ at 25°C found in the literature on VO_x ,¹⁻⁴ and in fact higher than most TCRs reported in undoped VO_2 films.¹⁹ We ascribe this to our samples being an essentially pure VO_2 phase. From Eq. (6), $E_g=2\beta kT^2$, and substituting $\beta=0.035$ and $T=25+273.1=298.1\text{ K}$, we obtain $E_g=0.54\text{ eV}$, in fair agreement with the bandgap value in VO_2 single crystals.²⁰

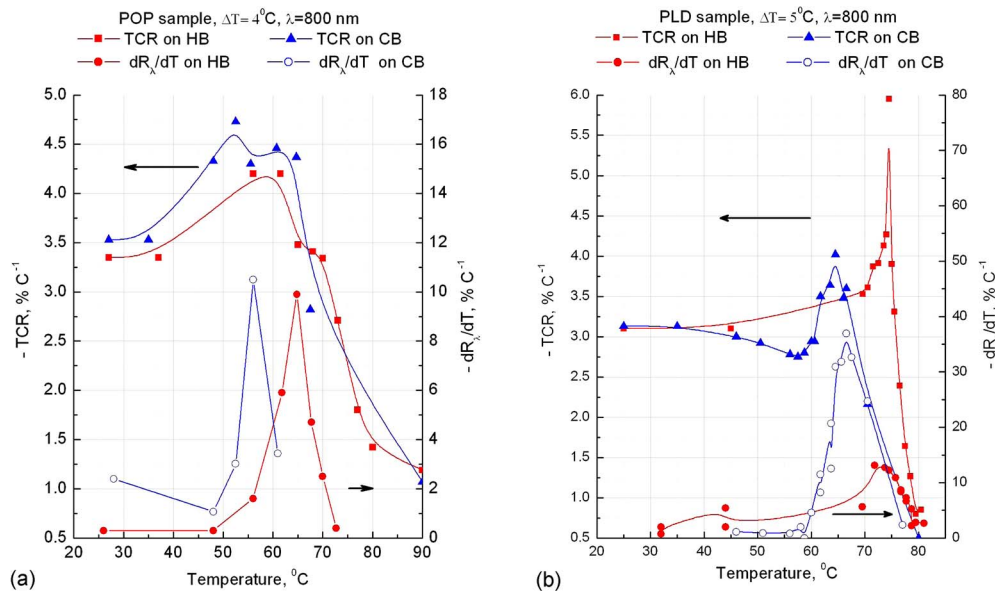


FIG. 5. (Color online) TCRs and optical reflectivity slopes in pure S-phase and in various NHBs vs T_0 . (a) POP sample of Fig. 3(a) and (b) PLD sample of Fig. 3(b). On both graphs, when available, color red indicates a HB and blue indicates a CB.

The main feature of the data shown in Figs. 5(a) and 5(b) is the nonmonotonous, peaked TCR versus T_0 dependence in both POP and PLD samples. Although the peak shape is different for the two types of samples, the gross features are common: TCR starts from an S-phase value at 25 °C, rising with increasing T_0 by 36% to a peak value of 4.75% °C⁻¹ on the CB in a POP sample, and by 92% (almost doubling) to a maximum TCR of 5.95% °C⁻¹ in a sharp peak on the HB in a PLD sample. At higher T_0 , when T_0 reaches to within 15–20 °C of the upper merging point T_M of the ML, TCRs drop down in both POP and PLD samples.

There can be seen some fine structure in this data: for example the peak in TCR on a CB of the PLD sample appears after a shallow minimum; there is a suggestion of a double-peaked structure in the POP data. We re-measured the PLD sample several times, with increased number of NHBs, and confirmed that the sharp peak and fine structure seen in Fig. 5(b) are real. However, in this paper we will be satisfied with explaining the gross features, leaving the fine structure explanation for the future.

We note that TCRs among different NHBs do not change as $1/T_0^2$ as would be predicted by Eq. (6); apparently, this dependence is masked by other, stronger effects which are at work here, as will be discussed below.

Apart from the *accommodation* behavior in the initial measurements which was mentioned in Sec. III, NHBs and their TCRs remain stable and reproducible after multiple cycling. This includes repeated excursions back and forth about a midpoint of a given NHB. We can also go out on a global trip over the entire ML, come back to (approximately) the same attachment point T_0 , and once more effect a small backward excursion, tracing an NHB with the same TCR as before the global trip.

To summarize resistive NHB properties:

- NHB can be initiated from any attachment temperature T_0 on a ML.
- Postaccommodation NHB is reproducible upon repeated back-and-forth temperature excursions.
- NHB is linear in $\log(\rho)$ versus T .
- TCR measured in various NHBs, when plotted versus attachment temperature T_0 , exhibit a peak, with the highest TCR values exceeding the S-phase 25 °C value by 36% in a POP sample and by 92% (almost doubling) in a PLD sample, exhibiting at the peak a high TCR value of 5.95% °C⁻¹.
- All TCR values fall off when T_0 approaches T_M .

VI. NHBs IN OPTICAL REFLECTIVITY

Although in this paper we place an emphasis on resistive properties, we will briefly discuss our optical data as well, as they also show a similar nonhysteretic behavior (optical reflectivity NHBs). We believe these data shed additional light on the theoretical picture we propose (see Sec. VII). The optical NHBs may be of interest for the proposed optical readout scheme,²¹ which we are not discussing here.

In a thin film with thickness comparable to the wavelength of light, the Fabry-Perot reflectivity exhibits a deep

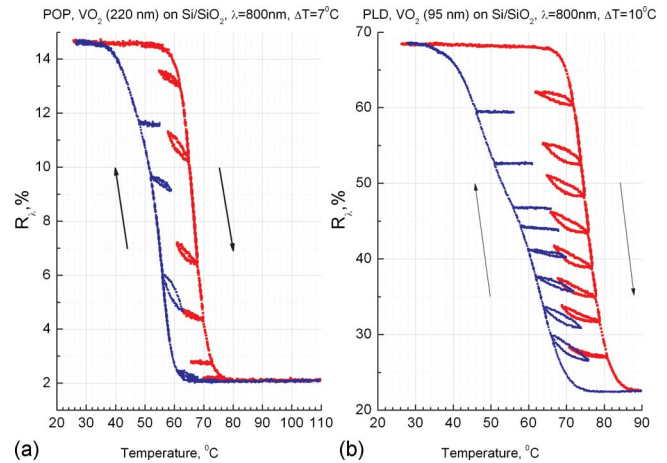


FIG. 6. (Color online) Major hysteresis loops in optical reflectivity with minor loops of (a) POP with $\Delta T=7$ °C and (b) PLD with $\Delta T=10$ °C. All data taken with 5 °C/min ramp rate; these are the same samples as in Figs. 1–3.

destructive interference minimum as a function of wavelength λ_0 when $m+1/2$ ($m=0, 1, 2, \dots$) wavelengths $\lambda = \lambda_0/n$ fit into an optical path inside the material of refractive index n . At normal incidence, the condition becomes $2d = (m+1/2)\lambda_0/n$. The wavelength corresponding to a minimum in reflectivity is $\lambda_{0 \text{ min}} = 2nd/(m+1/2)$. As n in VO₂ is changing between n_S in a semiconducting phase and n_M in a metallic phase upon heating, the position of the minimum $\lambda_{0 \text{ min}}$ will shift. In VO₂ this shift is significant in the visible range and is even larger in the IR range. It should be noted that, in addition to n , the absorption coefficient is also changing in the phase transition, further influencing reflectivity. The hysteresis in $n(T)$ has the same origin as the resistive hysteresis. As a result, the optical reflectivity $R_\lambda(T)$ in VO₂ is also hysteretic, with the shape and orientation of the hysteresis curve depending on the wavelength of light at which it is measured.⁹

In Figs. 6(a) and 6(b) we show major and minor hysteresis loops in optical reflectivity $R_\lambda(T)$ of our POP and PLD films, with long excursions of 7 and 10 °C, respectively (i.e., this is an optical analog of Fig. 2). These data were measured at $\lambda=800$ nm; the choice of λ influences the shape and orientation of the major hysteresis loop, but it does not change the behavior of minor loops we will be describing here. The optical data is somewhat noisy due to significant instrumental noise encountered in the Ocean Optics spectrometer, but sufficient for observing the overall behavior.

In Fig. 6 we see minor loops, some of them degenerating into optical NHBs, just like in resistivity in Fig. 2. Additionally we see that some minor loops are T -dependent, while others are not. In Fig. 7 we plot data for the same samples with short excursions of 4 and 5 °C respectively (i.e., this figure is an optical analog of Fig. 3).

We see that all minor loops degenerate into NHBs in Fig. 7, in complete analogy to Fig. 3. Some of these NHBs are T -dependent, others are not. We note that those which are T -dependent correspond to hysteretic minor loops in Fig. 6, while T -independent NHBs correlate with nonhysteretic be-

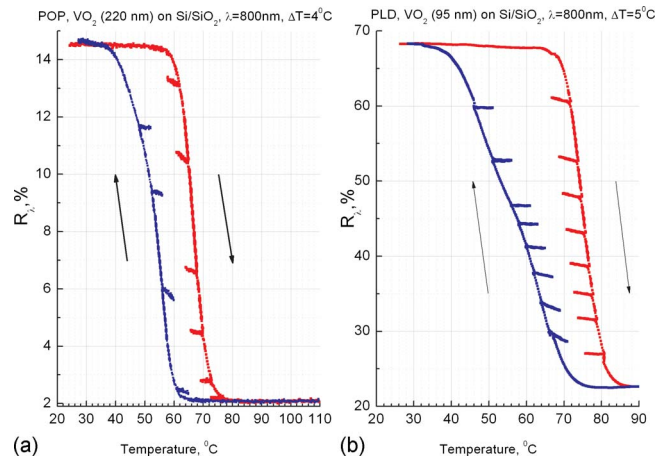


FIG. 7. (Color online) Major hysteresis loops in optical reflectivity with minor loops of (a) POP with $\Delta T=4^\circ\text{C}$ and (b) PLD with $\Delta T=5^\circ\text{C}$. All data taken with $5^\circ\text{C}/\text{min}$ ramp rate; these are the same samples as in Figs. 1–3 and 6.

havior in Fig. 6. We will explain this correlation in Sec. VII. In Fig. 8 we show a single optical NHB on an expanded scale (this is optical analog of Fig. 4).

It is interesting to compare data on reflectivity and resistivity measured simultaneously from the same sample area, which was done in our setup, as was described in Sec. II. In Fig. 9 we show such superimposed data for a PLD sample.

Looking at Fig. 9 we note that the two ML shapes are almost identical. Of course, resistivity is on a logarithmic scale, while reflectivity is on a linear scale, so they are as identical as apples and oranges can possibly be. In resistive curves we observe semiconducting TCR below the transition and in NHBs. Many (not all) of the optical NHBs too show a strong T -dependence, imitating resistive TCR in appearance. We note that, in contrast to the agreement seen in the PLD data in Fig. 9, in our POP film optical and resistive hysteresis loops [which can be seen separately in Figs. 2(a) and 7(a)] have a different shape and, when superimposed (not shown), appear shifted with respect to each other by a few degrees. A similar temperature offset of a few degrees had been observed and explained in Ref. 22. The appearance and the degree of such an offset between optical and resistive transitions are related to a requirement of percolation for the re-

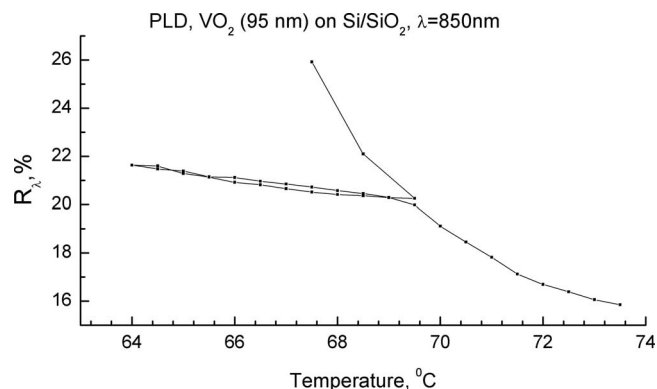


FIG. 8. Optical reflectivity NHB attached at $T_0=69.5^\circ\text{C}$ on the HB of the major hysteresis loop shown on an expanded scale (PLD sample measured at $\lambda=850\text{ nm}$ in a Perkin-Elmer spectrometer, ramp rate $0.5^\circ\text{C}/\text{min}$).

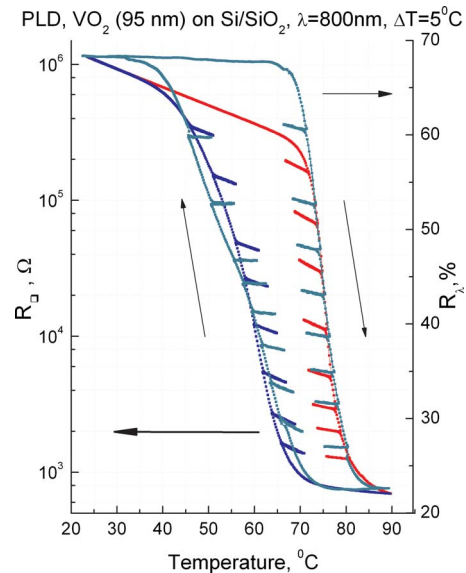


FIG. 9. (Color online) Resistivity and optical reflectivity major hysteresis loops of a PLD sample superimposed. If color is available: HB resistivity shown in red, CB in blue, reflectivity all shown in green; $\Delta T=5^\circ\text{C}$ and ramp rate $5^\circ\text{C}/\text{min}$ in both types of data.

sistive transition to take place, while an optical transition depends on the relative area coverage of the two phases. The details depend on the grain size and on film thickness; we will not address these issues here.

Optical slopes dR_λ/dT are plotted versus T_0 in Figs. 5(a) and 5(b) alongside TCR, with TCR scales on the left and dR_λ/dT scales on the right of each figure. We will discuss their relationship in Sec. VII.

We believe we understand why resistive NHBs exhibit T -dependence: it is essentially the TCR of a semiconducting phase (see Sec. VII below). But why do we see T -dependence in many of the optical NHBs? This observation suggests to us that there must be a T -dependent area redistribution between the S and M phases within a NHB. Indeed, Fabry-Perot optical reflectivity, being mainly determined by the refractive index, should be sensitive to the ratio of the total areas of S and M domains, and not to their connectivity (topology), while resistivity is predominantly sensitive to the topology, and only to a lesser degree depends on the ratio of the areas.

In the absence of optical data, looking at the resistivity alone, one may assume that S and M domains within NHB are “frozen,” that the geometry of S and M domains does not change at all within a NHB. In such a picture, resistivity variation within a NHB would solely reflect the semiconductor resistivity of a percolating S-phase. But looking at the optical data shown here, we must conclude that in T -dependent NHBs, the relative areas occupied by the S- and M-phases are changing within a NHB and the domain structure is not frozen. This requires a more refined topological picture presented in Sec. VII.

VII. AN EXPLANATION OF THE NHB PHENOMENA AND OBSERVED RESISTIVE-OPTICAL CORRELATIONS

Let us now give a qualitative explanation to the observed NHB phenomenon. We wish to qualitatively understand both

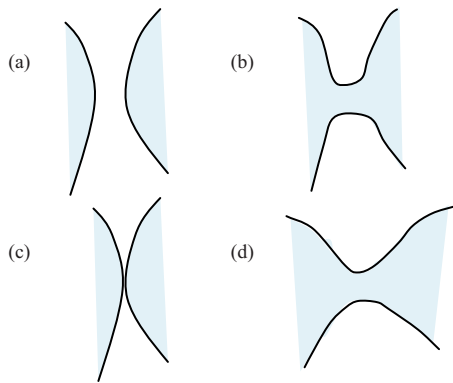


FIG. 10. (Color online) Semiconductor-metal boundary; metallic phase is shown shaded. Top row [(a) and (b)] corresponds to temperature T_1 and the bottom row [(c) and (d)] to temperature $T_2 > T_1$.

the nonhysteretic behavior and the fact that all NHBs have similar TCR that is essentially the S-phase TCR. We also need to reconcile our explanation with the fact that optical NHBs (at least some of them, see Figs. 6–9) have T -dependence as well. We will tie this optical behavior to the observed peaked TCR versus T_0 curve.

The hysteretic region in VO_2 is a mixed state consisting of both the semiconductor (S) and the metallic (M) phase regions. Each such region located in a film around a point with spatial coordinates (x, y) transitions into the other phase at its own temperature $T_C(x, y)$ which is continuously distributed in a macroscopic sample. At a given temperature T inside the hysteretic loop, some parts of the film have $T_C(x, y) < T$ and some $T_C(x, y) > T$. In the first approximation, the boundary wall between the S and M phases is determined by the condition $T_C(x, y) = T$. In this approximation, the wall is highly irregular and its ruggedness corresponds to the scale at which one can define the local $T_C(x, y)$. On closer inspection, however, we need a refinement that takes into account the *boundary energy*, associated with the phase domain wall itself. The boundary energy is positive and to minimize its contribution to the free energy the domain walls are relatively smooth.

For concreteness, let us consider the HB. As the temperature rises, the area of the M phase increases. Let us focus on two metallic lakes that are about to merge.

Since the boundary is smooth, at some temperature the distance between the lakes becomes smaller than the radius of curvature of either lake at the point they will eventually touch. Therefore, at some $T = T_{\text{cr}}$ the following two configurations will have equal energies: one comprising two disconnected M phase lakes that are near touching, but not quite, and the other with a finite link formed, Figs. 10(a) and 10(b), respectively. Both configurations are characterized by equal boundary lengths and therefore have equal free energy. In the thermodynamic sense one could call the T_{cr} the critical temperature for the link formation, if we could wait long enough. The actual transition forming a local link, however, does not occur at that temperature because of an immense *kinetic* barrier between these two macroscopically different configurations. The transition occurs at a higher $T_0 = T + \Delta T^*$ when it is actually forced, i.e., when the two phases

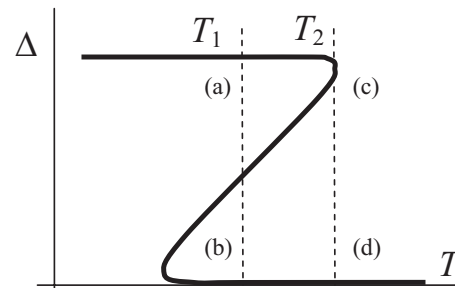


FIG. 11. Order parameter characterizing the local transition in a certain region, including contribution of the boundary energy. At temperature T_1 the two phases have equal energies. By definition, the local $T_C(x, y) = T_1$. The actual transition occurs at $T_2 > T_1$ and corresponds to the formation of a finite link, as in Fig. 10(d).

touch at a point. We associate the steep slopes of the ML with the quasicontinuous formation of such links, i.e., with local topological changes. On the HB the steep slope is associated with the merger of metallic lakes; on the CB it is the linkage of semiconductor regions.

Consider now a small excursion backward from T_0 . As the temperature decreases, the last formed M-link does not disappear immediately for the same kinetic reason. One has two S regions that need to touch in order to wipe out the M-link. It takes a backward excursion of amplitude ΔT^* to establish an S-link and thus disconnect the last M-link. So long as we are within ΔT^* , i.e., stay on the same NHB, the area of S and M domains changes continuously, but the topology is stable and no new links are formed. Within the range of that stable “frozen topology,” the resistivity of NHB is predominantly controlled by the percolating semiconductor phase.

The local transition is further illustrated in Fig. 11, which depicts an order parameter Δ that characterizes the transition; $\Delta = 0$ in the metallic phase and finite in the semiconductor phase. The points (a) to (d) correspond to the configurations in Fig. 10.

If we now cool the sample a little, the local region will follow the lower branch of the curve, will pass point (b) and undergo transition at the leftmost knee. That transition corresponds to establishment of a link between the top and the bottom *semiconductor* phases, as illustrated in Fig. 10. The temperature range of the transitionless cooling corresponds to shrinkage of the metallic region *without* a local topological change. The described picture is the basis of our interpretation of the slopes in the hysteretic $\rho(T)$ loop (see Fig. 3).

The slope (TCR) on the NHB may be somewhat higher than that of the semiconductor phase itself because it includes not only the temperature variation of semiconductor resistivity but also the smooth change of geometry. Indeed, looking at Fig. 5 where we plotted TCRs and optical slopes dR_λ/dT on the same graph, we observe that the peak in dR_λ/dT takes place in the same temperature interval in which we observe the peak in TCR. Higher values of dR_λ/dT imply the higher rate of area redistribution between the S- and M-phases within a NHB. Let A_S and A_M be the total areas of S-phase and M-phase in a sample, so that the total sample area is $A = A_S + A_M$. Clearly, as A does not depend on T , $dA_M/dT = -dA_S/dT$, i.e., the area of one phase grows at

the expense of the other. The optical slope dR_λ/dT is proportional to this area redistribution slope, and the maximum in dR_λ/dT reflects the maximum in dA_M/dT . This proportionality is true for the slopes on a ML as well as for smaller slopes we find in NHBs. When temperature is increasing, in all cases M-phase either grows or stays the same, $dA_M/dT \geq 0$; equal sign here corresponds to those NHBs with “frozen geometry.” Increasing M-phase content promotes electrical conductivity (lowers resistivity), and therefore TCR in NHBs corresponding to nonzero dR_λ/dT should be enhanced compared to the pure S-phase, and the maximum in dR_λ/dT should correlate with the maximally enhanced TCR. Figure 5 confirms this correlation for both types of samples, although the shape of the peaks in TCR and in dR_λ/dT is not identical.

The percolation picture also helps to understand why dR_λ/dT will exhibit such a maximum in the first place. With changing temperature, the boundary moves, each section of the boundary line advancing in the direction normal to this line at any given temperature. It is clear that the highest rate of change in the area of each phase will therefore occur when the boundary is the longest, i.e., at the percolation transition. Thus the observed peak in dR_λ/dT occurs right at the percolation transition, allowing its detection. The considerations expressed above for a HB apply equally to a CB of the ML.

We can further see why temperature intervals where $dR_\lambda/dT \approx 0$ in Figs. 6 and 7 are also the same temperature intervals in which minor loops tend to become nonhysteretic, degenerating into NHBs more readily than the other loops. Indeed, as we already observed, $dR_\lambda/dT \approx 0$ implies $dA_M/dT = -dA_S/dT \approx 0$, or constant areas of S- and M-phases. Hysteresis is associated with delayed transformations of one phase into the other. In the absence of such transformations there is no hysteresis.

In summary, we explained why there exists a threshold excursion length ΔT^* below which all minor loops become NHBs; in our samples $\Delta T^* = 4-5$ °C. As long as the S-phase forms a global cluster (and therefore the M-phase is disconnected), the S-phase TCR will be observed in the NHBs. A secondary but noticeable, interesting, and potentially beneficial effect is the increase of TCR values above the S-phase value due to redistribution of S- and M-phase areas within an NHB. This effect is strongest when the boundary line between the two phases is the longest, i.e., at the percolation transition. At higher temperatures, above the percolation transition, the M-phase percolates, shorting out the S-phase, and TCRs fall to low values.

Finally, the vanishing optical slope $dR_\lambda/dT = 0$ indicates “frozen” geometry of S- and M-phases and thus signals a condition that promotes minor loops degenerating into NHB even at $\Delta T > \Delta T^*$.

VIII. UFPA TECHNOLOGY WITH MICROBOLOMETERS IN A NHB REGIME

A. Main benefits; Choosing the operating temperature

We propose that NHB phenomenon can be beneficially employed in UFPA applications. One can now make use of a good quality, single phase VO₂ material instead of a mixed oxide VO_x to fabricate the pixilated bolometric sensor array.

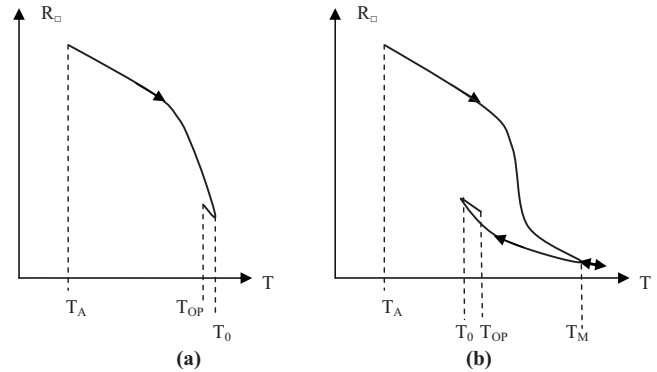


FIG. 12. A schematic diagram showing steps which have to be taken to reach T_0 from room temperature T_A when (a) T_0 is on a HB and (b) T_0 is on a CB.

The deposition process for VO₂ is compatible with the normal bolometer fabrication process: using POP we deposited good VO₂ at below 400 °C.⁹ Despite using VO₂, hysteresis is eliminated when a sensor array operates within a NHB attached either to the HB or to the CB. The NHB will be chosen on the basis of its desired resistance, which can be adjusted in a wide range in order to be matched to the read-out circuit amplifier. The resistance will be considerably smaller (up to two to three orders of magnitude) than the unacceptably high resistance at 25 °C discussed in Sec. II. NHB will be also chosen to maximize TCR, which, as we have seen in Sec. V, varies between different NHBs around the ML, peaking at the percolation transition, with values as high as 6% °C⁻¹. The operating temperature T_{OP} (i.e., the temperature at which the sensor array is stabilized awaiting the projected IR signal) will be chosen within a NHB; either near one of the ends or in the middle of the available range (total NHB width) $\Delta T^* = 4-5$ °C. Because of the hysteresis, the process of reaching T_{OP} starting from room temperature requires performing specific heating and cooling steps depicted schematically in Fig. 12(a) and 12(b) for the T_0 on a HB and on a CB, respectively.

Positioning an array at T_{OP} will require: on a HB, warming up to T_0 and cooling down to T_{OP} ; on a CB, warming up to above T_M , cooling down to T_0 , and again warming up to T_{OP} . If T_{OP} is chosen in the middle of a NHB, the last step requires cooling down from T_0 to $T_0 - \Delta T^*/2$ on a HB, and warming up from T_0 to $T_0 + \Delta T^*/2$ on a CB.

B. Increased absorptivity

While the main benefits of NHB regime are adjustable R and increased TCR, another, less significant benefit of operating in NHB regime instead of at 25 °C is in increased IR absorption. As was mentioned in the Introduction, in UFPA technology it is necessary to enhance IR absorption by creating a quarter wave resonator under the suspended microbolometer;¹⁻⁴ otherwise VO_x in the S-phase and other bridge structures (principally Si₃N₄ bridge material) do not absorb enough IR radiation. By its very nature, such a resonator can enhance absorption only at one selected wavelength; $\lambda = 10$ μm is usually chosen. With such a resonator

in place, absorptivity in the 8–14 μm band reported in the literature on UFPA technology varies from $\eta=0.5$ to $\eta=0.8$.¹⁻⁴

In a NHB regime, the sensor is part semiconductor and part metal; the closer is the chosen NHB to the metallic end of the transition, the higher will be the M-fraction. This should increase η because while S-phase is almost perfectly transparent in the IR range M-phase is opaque.

Let us consider this in more detail. Absorption coefficient γ is defined through $P_{\text{tr}}=P_{\text{inc}}e^{-\gamma d}$, where P_{inc} and P_{tr} are the incident and transmitted radiant powers, and d is sensor thickness. Absorptivity η is the fraction of incident power absorbed in a sensor. Neglecting power reflected back from the sensor $\eta=(P_{\text{inc}}-P_{\text{tr}})/P_{\text{inc}}=1-e^{-\gamma d}$.

Detailed measurements of $\gamma(\lambda)$ in the two phases were performed in Ref. 23, where it can be seen that $\gamma(8 \mu\text{m})$ and $\gamma(14 \mu\text{m})$ are, respectively, 100 times and 10 times higher in the M-phase than in S-phase. In the approximate middle of this interval, at $\lambda=10 \mu\text{m}$, $\gamma_S=0.2 \mu\text{m}^{-1}$, and $\gamma_M=10 \mu\text{m}^{-1}$,²³ and we find for a VO_2 layer with $d=50 \text{ nm}$, if it were 100% in the S-phase, $\eta=0.01$ (almost perfect transparency to IR radiation), while if it were 100% in M-phase, $\eta=0.39$. Thus, even in such a thin layer, approximately 40% of incident IR radiation will be absorbed in M-phase VO_2 . (We note that for a twice thicker layer with $d=100 \text{ nm}$, $\eta=0.63$). Of course, in a NHB only part of the VO_2 layer is in M-phase. Still, the effect may be significant enough to provide an improvement in microbolometer IR absorption, or to ease requirements for the construction of a quarter-wave resonator. Detailed calculations and modeling relating to this perceived benefit are beyond the scope of this paper. Increased η will increase R_V and decrease NETD. For the sake of our estimates in this section and in Sec. IX we will arbitrarily assume that, keeping all the features of the existing UFPA technology, such as the resonator structure, and additionally working in the NHB regime, we can achieve $\eta=0.9$.

C. Decreased latent heat

The first-order phase transition in VO_2 is accompanied by release/absorption of latent heat,⁸ which, together with hysteresis, caused concern for the VO_2 use as a sensor material in microbolometers.² It follows from the physical understanding put forward in this paper that VO_2 experiences fewer microdomain phase transitions per temperature interval ΔT within a NHB than on the ML. It seems plausible that the latent heat $Q_{\text{NHB}}(\Delta T)$ released/absorbed when temperature changes by ΔT within a NHB will be much smaller than the latent heat $Q_{\text{ML}}(\Delta T)$ released/absorbed in the same temperature interval on the ML. Specifically, we expect their ratio $Q_{\text{NHB}}(\Delta T)/Q_{\text{ML}}(\Delta T)$ to be the same as the ratio of area-redistribution rates $(dA_M/dT)_{\text{NHB}}/(dA_M/dT)_{\text{ML}}$, which in turn is equal to the ratio of optical slopes $(dR_\lambda/dT)_{\text{NHB}}/(dR_\lambda/dT)_{\text{ML}}$ (see Sec. VII). The latter ratio can be measured (see Fig. 7), being at least ten times lower for the “interesting” NHBs (those also having high TCR) than on the ML.

D. Does the narrow operating range of a few degrees present a problem?

A VO_x sensor operating at 25 °C has a wide range (tens of degrees) of temperatures above 25 °C in which semiconductor resistivity is approximately linear in $\log(\rho)$ versus T . For a VO_2 sensor operating in a NHB regime the available range of temperatures is more limited $\Delta T^*=4-5 \text{ }^\circ\text{C}$.

There are two sources of a temperature change in a pixel: exposure to a scene (target) and pulsed readout. When target temperature changes by ΔT_t , sensor temperature changes by ΔT_s . Somewhat surprisingly, we could not find the actual values of ΔT_s anywhere in the available literature. It is however possible to estimate this parameter from the given values of responsivity, TCR and incident IR power.¹⁻⁴ It appears that in a typical UFPA sensor $\psi=\Delta T_s/\Delta T_t \sim 0.01$. This would imply that in our case, with sensor operating close to the lower temperature end of a NHB, the NHB being at 60–70 °C, the target temperature would have to exceed $\sim 500 \text{ }^\circ\text{C}$ for the ΔT_s to exceed $\Delta T^*=4-5 \text{ }^\circ\text{C}$.

We also estimated ΔT_s directly, using blackbody radiation calculations in the following way. A sensor (pixel) having an area $A=50 \times 50 \mu\text{m}^2=2.5 \times 10^{-9} \text{ m}^2$ is at $T_s=65 \text{ }^\circ\text{C}=338 \text{ K}$, surrounded by objects at the same temperature (walls of a chamber, substrate, optics, etc.). This sensor is in the focal plane of IR optics with $F/\#=1$ (which implies solid angle of $2\pi/5$ steradians), with IR signal from a target projected upon a sensor in the 8–14 μm spectral interval. The target is represented by an infinite plane at temperature $T_t=438 \text{ K}$, taken to be 100° higher than T_s . All emissivities are taken to be equal to 1 (blackbody), and optics is considered perfectly transparent in this interval. Under these conditions, the IR power delivered to a sensor $P'=3.81 \times 10^{-7} \text{ W}$.²⁴ At the same time, the sensor radiates power out, in a solid angle of 2π . In all directions outside of the solid angle $2\pi/5$ there is thermal equilibrium for all wavelengths. Further, we assume that for all wavelengths outside of 8–14 μm interval there is thermal equilibrium in the full hemisphere 2π . In a solid angle in which it is exposed to IR signal, however, sensor radiates back less than it receives. The power radiated back into a $2\pi/5$ solid angle by a sensor at 338 K, in the 8–14 μm interval, can be also calculated,²⁵ it is $P''=1.45 \times 10^{-7} \text{ W}$. The difference is $P_{\text{IR}}=P'-P''=2.35 \times 10^{-7} \text{ W}$. We note that this power is almost exactly the same as the value given in Ref. 3 for the incident power on a $50 \times 50 \mu\text{m}^2$ detector from a target at 120 °C, giving us some confidence in the correctness of this calculation. We further note that, according to Ref. 3, the sensor response ΔT_s is essentially linear in P_{IR} , confirming that our ψ is a constant.

Inserting $P_{\text{IR}}=2.35 \times 10^{-7} \text{ W}$ into Eq. (1), in which we are also taking $\eta=0.9$ and typical values¹⁻⁴ $G=10^{-7} \text{ W/K}$, $\tau_{\text{th}}=10 \text{ ms}$, $f_{\text{fr}}=30 \text{ Hz}$, $\omega=2\pi f_{\text{fr}}=188.5 \text{ s}^{-1}$, we find $\Delta T=1 \text{ K}$. This calculation, therefore, confirms that $\psi \approx 0.01$.

A word of caution about using Eq. (1): this formula calculates the amplitude of a temperature increase ΔT_s for a sensor subject to sinusoidally modulated incident radiation flux. In reality IR flux is supplied in short pulses which are

much shorter than the frame period, e.g., 25–50 μs .^{1–4} Taking this into account and making more detailed calculations is beyond the scope of this paper.

The second reason for a pixel temperature change comes from a pulsed readout, either current-biased or voltage biased. In this case temperature increase in a sensor ΔT_r can be estimated from Eq. (2). According to Ref. 26, short $\tau_r = 65 \mu\text{s}$ is chosen to limit pixel heating to about 1 °C. For a sensor with $C = 10^{-9} \text{ J/K}$ and $R = 10 \text{ k}\Omega$ this implies $I_b = 38 \mu\text{A}$ and $V_b = I_b R = 0.38 \text{ V}$. A heating by about 1° would not present a problem in our case. However, in many papers on UFPA technology^{1–4} we see much higher V_b of up to 5 V. Such V_b will produce pixel heating significantly higher than 1 °C. Thus at higher bias voltages readout may drive a NHB sensor outside of its operating range ΔT^* .

E. An alternative way of dealing with narrow operating range

The relatively narrow operating range, if it presents a problem, may be avoided altogether in an alternative approach²⁷ that requires no excursions from the operating temperature at all. Reference 27 describes the heat balancing design in which an electrothermal feedback cycle is used to maintain both the resistance and temperature at a constant value. Instead of directly detecting the temperature change by measuring changes in resistance, electric power is delivered to each detector pixel in such a way as to balance the heat absorbed from the target. As incoming radiation increases, the power needed to maintain a constant temperature decreases. The measure of said power difference provides information about heat input into the microbolometer from the scene. This approach was designed to avoid individual array calibration,²⁷ but it also appears very well suited for our NHB regime.

F. What happens when microbolometer exceeds NHB limits?

What if we inadvertently exceed ΔT^* and go out of a given NHB? If a temperature excursion larger than ΔT^* occurs in the forward direction, a sensor will move to a neighboring NHB which will have a very similar TCR, as illustrated in Fig. 13 which shows the experimental resistivity exhibiting two very closely spaced NHBs.

Of course, for a given ΔT_s the useful signal depends not only on TCR but on R as well, and the value of R will change when we move from one NHB to the other. In a constant voltage biasing scheme, $I = V_b/R$ and signal $\Delta I = (V_b/R^2)\Delta R$, where $\Delta R = \beta R \Delta T_s$, so that the signal becomes $\Delta I = \beta V_b \Delta T_s / R$. The system will continue its operation in a neighboring NHB with the same β as before. If such shift from one NHB to the other is a rare event, the change in R value can be treated as a scaling factor for the signal, which can be adjusted in software.

If we exceed the range covered by ΔT^* in the backward direction, NHB will become a rather flat minor loop. This also should not lead to large readout errors.

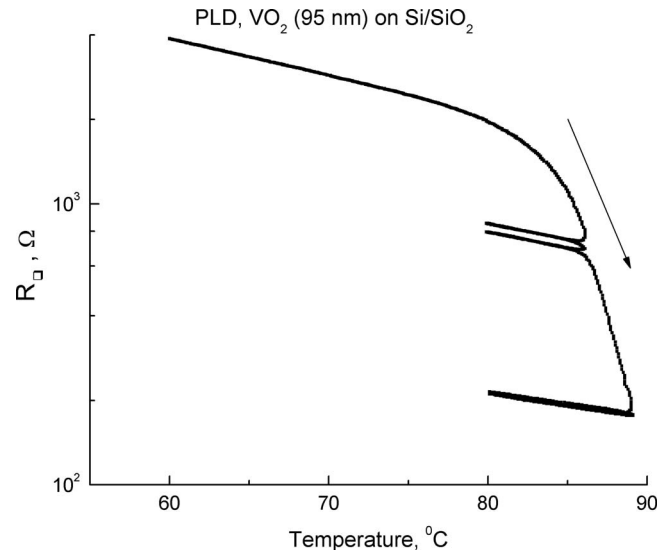


FIG. 13. A part of the ML with three NHBs in a PLD sample ($d = 95 \text{ nm}$); this sample is different from the one from which we presented most of the data above. Two NHBs can be seen being very closely spaced. Method 1 measurement with sweep rate of 0.5 °C/min.

G. Does the elevated temperature of operation present a serious problem?

In the UFPA VO_x -based technology, the array (substrate and microbridges) is stabilized at around 25 °C using thermoelectric systems with temperature stabilization of about 0.1 °C.³ In our scheme, the array will have to be stabilized with the thermocontroller at a T_{OP} which lies between 50 and 70 °C, just as in the existing technology it is stabilized at 25 °C. An array can be surrounded with objects at the same temperature T_{OP} , being in thermal equilibrium with its environment. This thermal environment may include walls of a chamber housing the sensor matrix, IR optics, the shutter (if it is employed), etc. Thermal equilibrium will be broken only during the time of sensor exposure to IR signal, as was described above. If the scene is warmer than the operating temperature, the exposure to the scene will heat the pixels; if colder, it will cool the pixels. The stabilization at 65 °C should not be more difficult than that at 25 °C.

There are known ways of lowering the operating temperature. Doping VO_2 by Mo, W, and Nb can significantly lower the transition temperature.²⁸ The interplay between benefits obtained by lowering the T_C and the deterioration of the phase transition generally observed with doping should be further studied. The T_C can be also dramatically reduced (even to slightly below room temperature!) while keeping the sharp transition by engineered strain.²⁹ However, this method requires growing ultrathin epitaxial films, which may not be practical in the UFPA application.

IX. ESTIMATES OF THE RESPONSIVITY AND SIGNAL TO JOHNSON'S NOISE RATIO

As stated in the Introduction, when estimating the figures of merit, we assume the sensor to be manufactured according to the best practices of the existing UFPA technology, having the same values of G and C as the existing VO_x microbolometers. The sensing layer, however, is a good qual-

TABLE I. Calculated R_V and upper bound estimates of NETD.

Sample, branch, NHB attachment temperature T_0	R in the middle of NHB (k Ω)	β ($^{\circ}\text{C}^{-1}$)	I_b (μA)	$R_V \times 10^5$ (V/W)	$V_n(\Delta f)$ integrated from measured spectrum (μV)	Unscaled NETD (mK)	Volume scaled NETD in a 50×50 μm^2 pixel (mK)
POP, HB, 67 $^{\circ}\text{C}$	14	0.034	150	3.01	4.44	6.22	262
POP, CB, 62 $^{\circ}\text{C}$	10.56	0.0445	150	2.97	3.29	4.7	196
PLD, HB, 74.4 $^{\circ}\text{C}$	33.1	0.0595	150	12.5

ity VO_2 operating in a NHB regime. As in Sec. VIII, we will take $G=10^{-7}$ W/K, $C=10^{-9}$ J/K (which implies $\tau_{\text{th}}=10$ ms), $f_{\text{fr}}=30$ Hz, and $\omega=2\pi f_{\text{fr}}=188.5$ s $^{-1}$. Inserting these ‘‘borrowed’’ quantities in Eq. (3) for responsivity, we obtain

$$R_V = 4.69 \times 10^6 I_b R \beta \eta. \quad (7)$$

Here the remaining factors are those of a sensor operating in a NHB regime. As stated in Sec. VIII, we assume $\eta=0.9$. The values of R_V thus calculated for two NHBs in a POP sample and for one NHB in a PLD sample are given in Table I. For $I_b=150$ μA , we obtain $R_V \approx 3 \times 10^5$ V/W in NHBs in a POP sample and $R_V=1.25 \times 10^6$ V/W in the highest β NHB in a PLD sample. In the existing UFPA technology based on VO_x , R_V does not exceed 2.5×10^5 V/W.¹

We also calculated signal to noise ratio (SNR) based on Johnson’s noise in our POP sample, as was done in Ref. 2, where SNR=416 was found in a VO_x sensor operating with 5 V bias. Owing to higher β and low R we found even better SNR in different NHBs, up to the maximum value of 1422. We are not providing the details of this calculation here, because in our case the excess $1/f$ noise significantly exceeds Johnson’s noise, at least at low frequencies.

X. NOISE MEASUREMENTS AND ESTIMATES OF NETD

Here we report an upper bound on the rms noise voltage V_n and estimate an upper bound on NETD. We leave a more detailed report sorting out the nontrivial details of noise behavior in VO_2 across the phase transition for the future publication.³⁰

Noise measurements in the spectral range from 10 to 7500 Hz were performed in the apparatus used in method 1, with pressed indium wires as contacts. Equipment included Agilent Spectrum Analyzer 4395A and Stanford Research Systems low noise preamplifier SR560. Sample currents from 1 to 150 μA were supplied from a constant-current source. The background noise was determined either by shorting out the voltage leads inside the apparatus or by shorting the preamplifier input; this background noise level at each frequency was subtracted from the signal. The setup was calibrated by measuring noise properties of a simple resistor. The zero-current Johnson’s noise was measured in a 10 k Ω standard resistor. The ratio between calculated Johnson’s noise level and the measured one served to calibrate subsequent noise measurements in VO_2 . We verified the absence of frequency dependence in a Johnson’s noise measurement, and observed the appearance of an excess $1/f$

noise when said resistor was measured in the presence of a bias current. We encountered some extraneous inductive pickup in all noise measurements, with peaks in $V_n(f, 1$ Hz) at some of the multiples of 60 Hz. The largest peaks were manually removed from the data. There is no guarantee, however, that some additional induced signal did not get into our noise measurements. Additional noise could also arise from the use of pressed indium contacts. It is known that contact problems can contribute to noise level and that better results can be obtained with plasma cleaning of the VO_2 film surface before the application of a contact,³¹ which have not been done in our case. Therefore, we consider obtained values of the total noise in a wide frequency range as an upper bound for the true noise in our samples.

The mean square noise voltage measurement was performed in a large number of neighboring narrow frequency intervals (we used 3 Hz intervals and divided the result by 3). In this way one obtains noise spectral density $S_V(f)$, which is numerically equal to the mean square $V_n^2(f, 1$ Hz) in 1 Hz interval around frequency f . Numerical integration of this quantity provides total mean square noise voltage in a frequency interval $\Delta f=f_2-f_1$, and square root of that gives total noise voltage in Δf , $V_n(\Delta f)=[\langle V_n^2(\Delta f) \rangle]^{1/2}$.

We measured noise in our samples at 25 $^{\circ}\text{C}$ and in different NHBs. The noise spectra $S_V(f)=V_n^2(f, 1$ Hz) from 10 Hz to about 1000 Hz were having a classical $1/f^\alpha$ form with index α from 0.92 to 1.2; at higher frequency we observed significant deviations from this behavior (flattening out of the noise spectrum). As an example, in Fig. 14 we present $V_n(f, 1$ Hz) obtained on one of the NHBs in the range from 10 to 200 Hz; Johnson’s noise level is indicated by a dotted line.

Table I summarizes NHB parameters R and β , measuring current I_b , values of R_V calculated according to Eq. (7) with $\eta=0.9$, values of $V_n(\Delta f)$ obtained by numerical integration of noise spectral density in the frequency interval from 10 Hz to 7.1 kHz, and corresponding values of NETD calculated according to Eq. (4). We note that, for the given values of R , current of 150 μA corresponds to voltage drops of 2.1 V and 1.6 V in the two NHBs chosen, which is in the range of V_b values given in the UFPA literature. We also note that we are taking the widest possible bandwidth $\Delta f=1/(2\tau_r)$ corresponding to $\tau_r=70$ μs , while it is possible that in reality the measurement bandwidth will be considerably more narrow; for example, in Ref. 6 it is taken to be 320 Hz. Narrowing the measurement bandwidth will significantly reduce $V_n(\Delta f)$ and NETD.

We also need to point out that our measurements here

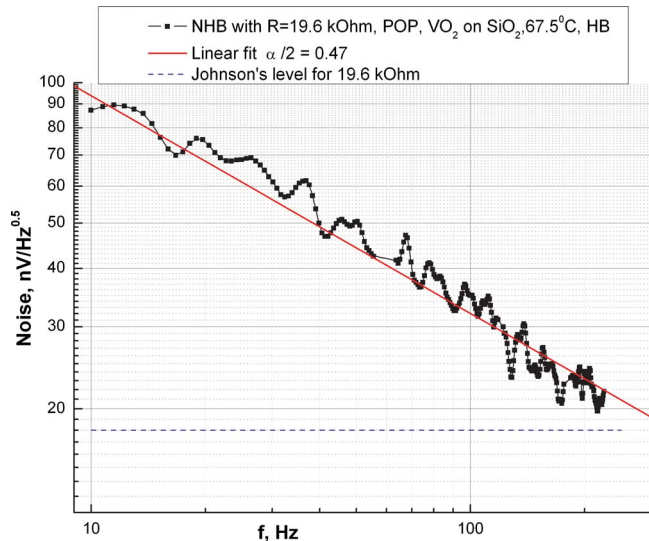


FIG. 14. (Color online) $V_n(f, 1 \text{ Hz})$ vs f for one representative NHB in a POP sample (parameters given in the inset). Straight red line represents the best fit to $1/f^{\alpha/2}$ law with $\alpha=0.94$. Dotted line is the Johnson's noise level at 67.5°C for $R=19.6 \text{ k}\Omega$.

are performed on $A \sim 1 \times 1 \text{ mm}^2$ VO_2 films, with $d = 220 \text{ nm}$ in a POP sample, while real array sensors would be somewhat thinner and much smaller, perhaps with $d = 50 \text{ nm}$ and $A = 50 \times 50 \mu\text{m}^2$. In the absence of the actual microbolometer data (which we hope to obtain one day) we can try to scale the results according to the square root of the volume ratio, in agreement with Hooge's scaling formula³² or with its recently proposed modifications.³³ This will increase $V_n(\Delta f)$ by a factor of $[v_{\text{pixel}}/v_{\text{sample}}]^{-1/2} = 42$. However, when we tried to observe this volume scaling in our samples by changing the volume by a factor of 10, we found that larger volume sample had larger noise, which directly contradicts Hooge's formula. The reasons for this discrepancy (poor contacts? volume dependence being different than predicted by Hooge's formula?) are not clear. This and other scaling issues will need to be further studied in the future. At this time we cannot be sure that such volume scaling is necessary. Thus in the last column of Table I we present an upper bound on volume-scaled NETD, with an understanding that this value may be significantly overestimated.

XI. OTHER OBSERVATIONS AND FUTURE DIRECTIONS OF RESEARCH

We noticed that the NHB width ΔT^* gets larger in wider hysteresis films. We have observed NHBs with ΔT^* up to 9°C in some samples (e.g., see Fig. 13). It will be interesting to study this relationship and to explore it for widening of the dynamic range for the benefit of the technology. We also noted above that ΔT^* may depend on the placement of a NHB inside a ML. This aspect also deserves further study.

The phenomenon of TCR increase in some NHBs above the S-phase TCR value (peak TCR of 5.95% in a PLD sample, and up to 4.75% in a POP sample) is of considerable interest. This line of enquiry will benefit from combining

resistive and optical measurements, the latter being an excellent guide in terms of finding the highest TCRs, as shown in this paper.

It may be of interest to study lightly doped VO_2 with an eye on lowering the transition temperature (or rather a range of transition temperatures in a hysteretic sample), thus decreasing the operating temperature of a proposed device. Simultaneously, it may be possible to further increase TCR in these doped samples.³⁴ It should be interesting to study other metal-insulator transition materials looking for NHB behavior in them as well.

Finally, study of noise in the hysteretic region requires more work. It would be particularly interesting to manufacture and evaluate a realistic UFPA prototype based on VO_2 sensors operating in the NHB regime and to evaluate its properties, including noise.

XII. SUMMARY AND CONCLUSIONS

We found an interesting shunting (shorting out) nanoeffect unique to a mixed system of low- and high-conductivity microdomains, such as found inside the hysteretic transition region of a phase-transitioning material VO_2 (other materials exhibiting metal-insulator or semiconductor-insulator transitions may also exhibit similar effects). This effect takes place only in the regime of interconnected (percolated) high-resistivity semiconducting phase. In this regime the partial shorting out of the S-phase by the M-phase provides for total low resistivity. Material becomes a semiconductor "sponge" with nanoscale metal enclosures. Because of the S-phase percolation, resistive T -dependence is largely unaffected, reflecting T -dependence of an S-phase. Moreover, a secondary effect of TCR enhancement due to redistribution of S-M areas within an NHB provides TCRs which can be considerably higher than in S-phase, in some cases almost doubling the room-temperature TCR value, with TCR up to 5%–6%. Further, it turned out that in limited temperature intervals this behavior is nonhysteretic, while taking place in the midst of the hysteretic transition region. Such unique *nanoshunted* material, while interesting in its own right, may be useful to the technology of IR visualization, as was argued in this paper. A similar effect exists in optical reflectivity.

We argue that certain advantages may be offered by these effects to the UFPA technology:

1. When a sensor operates in the NHB regime, it operates without a hysteresis, and this regime further provides simultaneous benefits of high TCR and low tunable R . The TCR in VO_2 at 25°C is higher than in VO_x , and a TCR in an NHB can be higher still (Fig. 5), whence we can expect higher bolometer responsivity. Using typical microbolometer thermal parameters and NHB electrical characteristics we calculated R_V of over 10^6 V/W (Sec. IX). Tunable R provides a way of matching to the electronic circuit amplifiers; low value of R reduces noise (Johnson's noise voltage is proportional to $R^{1/2}$; excess noise to R), and suppresses microbolometer heating during the resistive readout.
2. The VO_2 sensor material is well defined, both in terms of its stoichiometry (ratio of V to O in the VO_x formula)

- and in terms of its crystallographic phase. A well-defined single phase sensor material allows an easier process control, compared to the present technology's need to make reproducible uniform layers of mixed oxide VO_x .
3. The deposition process for the pure phase VO_2 is compatible with the normal bolometer fabrication process: for example, using POP, good VO_2 can be deposited at below 400°C .⁹
 4. A stand-alone sensor (without a resonant cavity) operating in a NHB, in a mixed state with considerable fraction of M-phase present, will have a much higher absorptivity η in the $8\text{--}14\ \mu\text{m}$ window than a sensor operating in S-state. Coupled with resonant cavity induced enhancement this promises absorptivity approaching 1.
 5. Operation in NHB regime largely removes a problem of latent heat release/absorption.
 6. Array nonuniformities and errors caused by exceeding NHB sensor operating range of about 5°C (corresponding to target temperature range of about 500°C) are made less detrimental by neighboring NHBs having the same TCR and being linear in $\log R$ versus T .

ACKNOWLEDGMENTS

We thank Dr. David Westerfeld for developing Laboratory View-based automated resistivity measurement system, Dr. Yuri Polyakov for his advice on noise measurements, Dr. Michael Gouzman for experimental advice and for lending some of the measuring equipment, Dr. Arsen Subashiev for useful theoretical discussions, and Dr. M. E. Levinshstein for providing us with unpublished manuscript of his work on Hooge relation. We also thank Dr. Peter Shkolnikov for his continuing interest and support of this work. This work was partially supported by the New York State Foundation for Science, Technology and Innovation (NYSTAR) through the facilities of the Center for Advanced Sensor Technology at Stony Brook.

- ¹R. Flannery and J. E. Miller, *Proc. SPIE* **1689**, 379 (1992); R. A. Wood and N. A. Foss, *Laser Focus World* **29**, 101 (1993); R. A. Wood, *Semicond. Semimetals* **47**, 43 (1997); A. Rogalski, *Prog. Quantum Electron.* **27**, 59 (2003).
- ²B. E. Cole, R. E. Higashi, and R. A. Wood, *Proc. IEEE* **86**, 1679 (1998).
- ³R. J. Herring and P. E. Howard, *Proc. SPIE* **2746**, 2 (1996).
- ⁴D. Murphy, M. Ray, A. Kennedy, J. Wyles, C. Hewitt, R. Wyles, E. Gordon, T. Sessler, S. Baur, D. Van Lue, S. Anderson, R. Chin, H. Gonzalez, C. Le Pere, S. Ton, and T. Kostrzewa, *Proc. SPIE* **5783**, 448 (2005).
- ⁵P. W. Kruse, L. D. McGlauchlin, and R. B. McQuistan, *Elements of Infrared Technology* (Wiley, New York, 1962).

- ⁶V. Yu. Zerov, V. G. Malyarov, and I. A. Khrebtov, *J. Opt. Technol.* **71**, 153 (2004).
- ⁷R. S. Scott and G. E. Frederics, *Infrared Phys.* **16**, 619 (1976).
- ⁸F. J. Morin, *Phys. Rev. Lett.* **3**, 34 (1959); N. Mott, *Metal-Insulator Transitions* (Taylor & Francis, London, 1997).
- ⁹M. Gurvitch, S. Luryi, A. Polyakov, A. Shabalov, M. Dudley, G. Wang, S. Ge, and V. Yakovlev, *J. Appl. Phys.* **102**, 033504 (2007) and references therein.
- ¹⁰R. A. Wood, U. S. Patent No. 5,450,053 (12 September 1995); H. Jeronimek, F. Picard, N. R. Swart, M. Renaud, M. Levesque, M. Lehoux, J.-S. Castonguay, M. Pelletier, G. Bilodeau, D. Audet, T. D. Pope, and P. Lambert, *Proc. SPIE* **2746**, 60 (1996); R. A. Wood, in *Uncooled Infrared Imaging Arrays and Systems*, edited by P. W. Kruse and D. D. Skatrud (Academic, San Diego, California, 1997), pp. 43–122; C. D. Reinsma, E. N. Grossman, and J. A. Koch, *Proc. SPIE* **3696**, 190 (1999).
- ¹¹G. Neto, L. A. L. de Almeida, A. M. N. Lima, C. S. Moreira, H. Neff, I. A. Khrebtov, and V. G. Malyarov, *Opt. Eng.* **47**, 073603 (2008).
- ¹²V. N. Andreev, B. P. Zakharchenya, Yu. S. Kapshin, V. A. Noskin, and F. A. Chudnovskii, *Sov. Phys. JETP* **52**, 684 (1980).
- ¹³V. Yu. Zerov, Yu. V. Kulikov, V. G. Malyarov, I. A. Khrebtov, I. I. Shaganov, and E. B. Shadrin, *Tech. Phys. Lett.* **27**, 378 (2001).
- ¹⁴Details of our PLD deposition process will be published separately.
- ¹⁵M. Gurvitch, S. Luryi, A. Polyakov, and A. Shabalov, "Non-hysteretic branches inside the hysteresis loop in VO_2 films for focal plane array imaging bolometers," <http://arxiv.org/abs/0805.3566>.
- ¹⁶F. M. Smits, *Bell Syst. Tech. J.* **37**, 711 (1958).
- ¹⁷L. A. L. de Almeida, G. S. Deep, A. M. N. Lima, and H. F. Neff, *Appl. Phys. Lett.* **77**, 4365 (2000); L. A. L. de Almeida, G. S. Deep, A. M. N. Lima, H. F. Neff, and R. C. S. Freire, *IEEE Trans. Instrum. Meas.* **50**, 1030 (2001).
- ¹⁸J.-G. Ramirez, A. Sharoni, Y. Dubi, M. E. Gomez, and I. K. Schuller, *Phys. Rev. B* **79**, 235110 (2009).
- ¹⁹A. Subrahmanyam, Y. Bharat Kumar Reddy and C.L. Nagendra, *J. Phys. D: Appl. Phys.* **41**, 195108 (2008), and references therein.
- ²⁰C. N. Berglund and H. J. Guggenheim, *Phys. Rev.* **185**, 1022 (1969).
- ²¹S. Luryi, M. Gurvitch, and F. Chudnovskiy, WIPO Publication WO/2002/099896, 2002 (available online from World Intellectual Property Organization at <http://www.wipo.int/pctdb/en/>).
- ²²J. Rozen, R. Lopez, R. F. Haglund, Jr., and L. C. Feldman, *Appl. Phys. Lett.* **88**, 081902 (2006).
- ²³J. A. Coath and M. A. Richardson, *Proc. SPIE* **3738**, 555 (1999). <http://www.sbfj.com/Flux/ExtBBcalc.html>
- ²⁴<http://hyperphysics.phy-astr.gsu.edu/Hbase/quantum/radfrac.html>
- ²⁵P. W. Kruse, *Proc. SPIE* **5406**, 437 (2004).
- ²⁶E. J. Lerner, *Laser Focus World* **37**, 201 (2001).
- ²⁷Y.-H. Han, K.-T. Kim, N. Chi-Anh, H.-J. Shin, I.-H. Choi, and S. Moon, *Sens. Actuators, A* **123–124**, 660 (2005); I. Takahashi, M. Hibino, and T. Kudo, *Jpn. J. Appl. Phys.* **40**, 1391 (2001).
- ²⁸K. Nagashima, T. Yanagida, H. Tanaka, and T. Kawai, *J. Appl. Phys.* **100**, 063714 (2006).
- ²⁹M. Gurvitch, S. Luryi, A. Polyakov, and A. Shabalov (unpublished).
- ³⁰A. P. Gruzdeva, V. Yu. Zerov, O. P. Konovalova, Yu. V. Kulikov, V. G. Malyarov, I. A. Khrebtov, and I. I. Shaganov, *J. Opt. Technol.* **64**, 1110 (1997).
- ³¹F. N. Hooge, *Phys. Lett. A* **29**, 139 (1969); F. N. Hooge, T. G. M. Kleinpenning, and L. K. G. Vandamme, *Rep. Prog. Phys.* **44**, 479 (1981).
- ³²A. P. Dmitriev, M. E. Levinshstein, and S. L. Romyantsev, *J. Appl. Phys.* **106**, 024514 (2009).
- ³³M. Pan, H. Zhong, S. Wang, J. Liu, Z. Li, X. Chen, and W. Lu, *J. Cryst. Growth* **265**, 121 (2004).